Metachronal coordination as a mesoscale phenomenon

Sebastian Ziegler,[1, a)] Megan Delens,[2, a)] Ylona Collard,[2] Maxime Hubert,[1, 3] Nicolas Vandewalle,[2] and Ana-Sunčana Smith[1, 3, 4]

[1)]*PULS Group, Institute for Theoretical Physics, Interdisciplinary Center for Nanostructured Films (IZNF), Friedrich-Alexander-Universität Erlangen-Nürnberg Cauerstr. 3, 91058 Erlangen, Germany*

[2)]*GRASP, Institute of Physics B5a, Université de Liège, 4000 Liège, Belgium*

[3)]*Group for Computational Life Sciences, Division of Physical Chemistry, Ruđer Bošković Institute, Bijenička cesta 54, 10000 Zagreb, Croatia*

[4)]*Center for Computational Advanced Materials and Processes, Department of Chemical and Bioengineering, Friedrich-Alexander-Universität Erlangen-Nürnberg Cauerstr. 3, 91058 Erlangen, Germany*

(*Corresponding authors: NV - nvandewalle@uliege.be, ASS - smith@physik.fau.de, asmith@irb.hr)

(Dated: 3 April 2026)

Metachronal coordination is a highly efficient natural strategy for swimming across scales, yet mimetic systems replicating this form of propulsion remain rare, limiting our ability to explore its underlying physics. Here, we investigate a minimal magneto-capillary system consisting of seven beads that exhibit metachronal-like motion when actuated by either a rotating or Lissajous-type oscillating magnetic field, resulting in net rotation or translation of the assembly, respectively. By systematically varying the driving frequency, we identify two distinct swimming regimes, both experimentally and theoretically. At low frequencies and negligible Reynolds numbers, propulsion arises from individual bead rotations phase-locked to the external field, constituting a linear, quasi-static regime. At higher frequencies, where the Reynolds number of the appendages exceeds unity, the dynamics transition to a deformation-dominated metachronal regime. Notably, optimized propulsion emerges near a mechanical resonance, underscoring the increasing role of inertia. While demonstrated on a specific design, we hypothesize that the existence of these regimes and the crossover between them may be a general feature of mesoscopic swimmers in nature.

I. INTRODUCTION

In living organisms, various locomotion strategies have evolved through natural selection, depending on the size and shape of the species, as well as the velocities they can achieve in their environment. Consequently, macroscopic organisms, like cetaceans or humans, rely on inertia to propel themselves, while microscopic swimmers, like bacteria or algae, are dominated by viscous dissipation. Because of these distinct interactions with the environment, different swimming strategies evolved. Organisms achieving large Reynolds numbers typically use cyclic strokes performed by their extremities, in combination with coasting, to move their bodies. At low Reynolds numbers, swimming requires non-reciprocal deformation of the organism's body or its appendages to overcome the fluid viscosity, which overdamps all coasting at this scale[1,2]. Interestingly, one strategy is employed by numerous organisms at all scales - metachronal coordination[3]. Metachronal coordination is a fascinating phenomenon in which the organism's periodically moving parts, such as limbs or appendages, operate in a sequential rhythm, slightly out of phase with one another. This results in a wavelike motion[4] that can be observed across the body of the organism. This behavior is widely observed in the cilia of microorganisms, such as Paramecium[5,6] and colonies of Volvox algae[7], where it facilitates swimming or fluid flow over their surface. Similar mechanisms are used in mammals, where metachronal strokes play a role in respiratory functions by transporting fluids along lung epithelia[8–10].

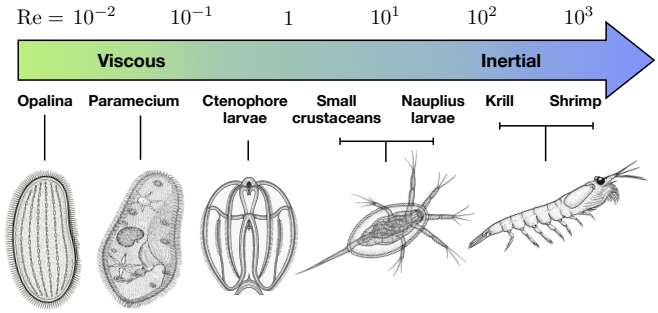

FIG. 1. Metachronal waves as an across-scales design principle for efficient swimming. Reynolds number is set by the characteristic size and velocity of the organism.

Metachronal waves are not exclusive to microscopic scale; they are also seen in larger organisms. For example, comb jellies (ctenophores) display iridescent waves as their ciliary rows beat metachronally, producing stunning shimmering colors through diffraction and interference of light[11]. Similarly, crustaceans, insects, annelids, and arthropods rely on such coordination for locomotion. Figure 1 highlights the diversity of organisms employing metachronal waves, covering a wide range of sizes and swimming speeds.

This ubiquity raises a fundamental question: Why has evolution favored metachronal waves across such diverse taxa and physical scales? The answer is likely found in their superior fluid transport and swimming efficiency compared to synchronous strokes[12–15]. Moreover, the versatility of metachronal coordination allows for various swimming modes, such as fast-forward swimming, hovering, and upside-down swimming, by adjusting stroke frequency and

[a)]These authors contributed equally to this work.

amplitude[16,17]. These properties make metachronal coordination a robust strategy in both natural and artificial swimmers.

The fascinating world of metachronal swimmers has inspired the development of bio-inspired robotic systems, particularly for underwater and interface locomotion. This inspiration has materialized in the form of magnetically actuated swimmers[18–26], and especially magnetocapillary assemblies as swimmers[27–32]. These devices, composed of soft-ferromagnetic particles trapped at a fluid interface, are held together at equilibrium distances through a balance of capillary attraction and magnetic repulsion[33]. When driven by time-dependent magnetic fields, they can reproduce metachronal coordination patterns[32]. However, the underlying mechanisms of these dynamics are not well understood.

An important hint about the underlying physics is provided by the theoretical generalization of bead assemblies[34–41]. Namely, by quantitative comparison of analytic approaches and experiments[31,42–44], we and others showed that magneto-capillary assemblies belong to the class of mesoscale swimmers, where the inertia of the beads has a considerable impact on its movement, while the inertia of the fluid remains subordinate[43,45,46].

Building on this experience in constructing and modeling bead-based swimmers, this study investigates the dynamics of magnetocapillary swimmers, depicted in Figure 2, under two distinct metachronal patterns: 1-arm and 2-arm metachronal coordination. We identify two kinematic regimes, one at low frequencies (0–1.5 Hz) and the other at high frequencies (3–5 Hz), each exhibiting a unique physical mechanism: the former is governed by hydrodynamic interactions, while the latter is dominated by bead inertia. Thus, we finally prove that, indeed, the mesoscopic regime is vital for efficient metachronous swimming.

II. INTEGRATED METHODOLOGICAL FRAMEWORK

A. Experimental setup

Using our expertise in magnetocapillary swimmers[28–32,47], we construct the device presented in Figure 2 consisting of a central bead of 800 μm in diameter, pinned at a water-air interface thanks to capillary effects. It is surrounded by six beads of 500 μm in diameter. All beads are made of chrome steel alloy AISI 52100 at density $\rho_b = 7.8\ 10^3$ kg/m^3. Although the alloy is considered to be a soft ferromagnetic, the particles exhibit a small remanent magnetization of the order of 100 A m^{-1}[48]. Therefore, the total moment of bead i is $\boldsymbol{\mu}_i = \boldsymbol{\mu}_{rem,i} + 4\pi a_i^3 \chi \boldsymbol{B}/(3\mu_0)$, with a_i and $\chi = 3$ being respectively the bead's radius and susceptibility, μ_0 the vacuum permeability, and $\boldsymbol{\mu}_{rem,i}$ the remanent moment.

The magnetic induction field $\boldsymbol{B}$ is applied on the device by three pairs of orthogonal Helmholtz coils, each providing up to 8 mT. The currents in the x- and y-coils are produced by an arbitrary function generator and a pair of amplifiers to propel the assembly eventually. The vertical field is typically constant at $B_v = 4.9$ mT. The imposed $\boldsymbol{B}$ field, therefore, yields a repulsive magnetic dipole-dipole force $\boldsymbol{F}^{\mathrm{m}}$ between the beads

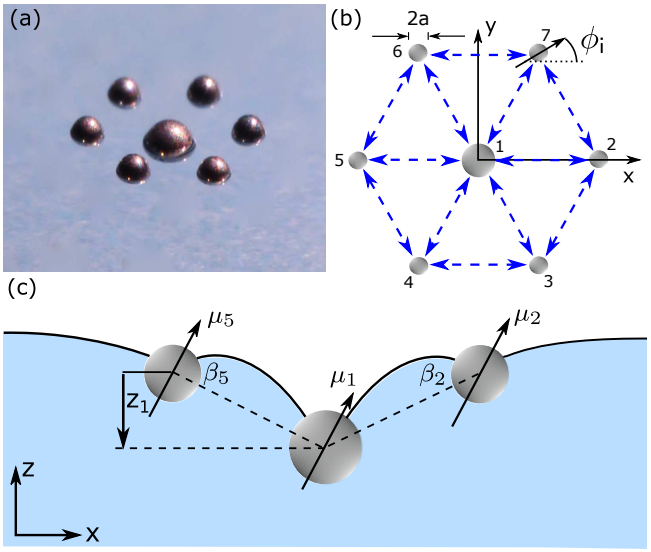

FIG. 2. **The magneto-capillary seven-bead assembly.** (a) Photography of the experimental device. (b) Sketch of the model for the seven-bead assembly. (c) Cut through the assembly along the x-direction, illustrating the vertical displacement of the central bead and the left-right asymmetric dipole-dipole interactions.

$$\begin{aligned}\boldsymbol{F}^{\mathrm{m}} = \frac{3\mu_0}{4\pi r_{ij}^4}\,[&(\hat{\boldsymbol{r}}_{ij}\times\hat{\boldsymbol{\mu}}_i)\times\hat{\boldsymbol{\mu}}_j \\ &+(\hat{\boldsymbol{r}}_{ij}\times\hat{\boldsymbol{\mu}}_j)\times\hat{\boldsymbol{\mu}}_i \\ &-2\hat{\boldsymbol{r}}_{ij}\cdot(\boldsymbol{\mu}_i\cdot\boldsymbol{\mu}_j) \\ &+5\hat{\boldsymbol{r}}_{ij}\cdot(\hat{\boldsymbol{r}}_{ij}\times\boldsymbol{\mu}_i)\cdot(\hat{\boldsymbol{r}}_{ij}\times\boldsymbol{\mu}_j)]\,,\end{aligned} \tag{1}$$

and a magnetic torque $\boldsymbol{T}^{\mathrm{m}}$

$$\begin{aligned}\boldsymbol{T}^{\mathrm{m}} &= \boldsymbol{\mu}_i\times\boldsymbol{B} \\ &+\frac{\mu_0}{4\pi r_{ij}^5}\left(3\boldsymbol{\mu}_i\times(3\boldsymbol{\mu}_i\cdot\boldsymbol{r}_{ij})\,\boldsymbol{r}_{ij} - r_{ij}^2\,(\boldsymbol{\mu}_i\times\boldsymbol{\mu}_j)\right).\end{aligned} \tag{2}$$

with $\boldsymbol{e}_{ij}$ the unit vector along $\boldsymbol{r}_{ij} := \boldsymbol{r}_j - \boldsymbol{r}_i$, and i, j bead indices.

Because the beads deform the water-air interface, they experience a lateral capillary force $\boldsymbol{F}^{\mathrm{c}}$[49], which takes the form

$$\boldsymbol{F}^{\mathrm{c}} = \frac{-2\pi\sigma}{l_c}\sum_i\sum_{j\neq i} q_i q_j K_1\left(|\boldsymbol{r}_{ij}^{\parallel}|/l_c\right). \tag{3}$$

Here $\sigma = 72$ mN/m is the water surface tension, K_1 is the modified Bessel function of the second kind of the first order, and $\boldsymbol{r}_{ij}^{\parallel}$ is the projection of $\boldsymbol{r}_{ij}$ on the xy-plane. Moreover, with g being the gravitational constant, and ρ the fluid density, $l_c = \sqrt{\sigma/g\rho}$ is the capillary length, which, for the water-air interface, is $l_c \approx 2.7$ mm. Finally, the capillary charge q_i represents the characteristic length of the vertical deformation of the liquid interface around each particle, which for the current case is around 12 μm for 500 μm beads and 45 μm for 800 μm beads[33,47]. This difference in q_i contributes to the

overall deformation of the interface as comprised in z_1 as depicted in Figure 2(c).

Capillary effects bind the beads strongly at the contact line with the liquid interface[31]. As a result, the beads mostly move in the xy-plane and rotate around the z-axis while experiencing repulsive magnetic interactions. The relative orientation to the x-axis is described by ϕ_i as sketched in Figure 2(b). This motion, together with the difference in capillary charge, will lead to asymmetric assembly deformation in a horizontal field, inducing device rotation and locomotion.

B. Equations of motion

To model the behavior of our device, we construct a bead assembly as shown in Figure 2. The beads explicitly experience capillary and magnetic forces as well as torques (Eqs. (1)- (3)). However, magnetic forces in the z-direction are neglected under the assumption that the capillary forces bind the particles at their contact line with the liquid interface, as suggested by experiments. For the hydrodynamic interactions between the beads, we use the bulk Rotne-Prager tensor. As previously shown by Ziegler et al.[41] in similar magneto-capillary systems, interface-resolved simulations indicate that bulk hydrodynamic approximations utilizing Rotne–Prager interactions, along with a properly rescaled drag coefficient, yield accurate predictions for interfacial systems in both low-Reynolds and mesoscopic regimes. We apply this approach here to effectively capture the essential hydrodynamic interactions that drive the dynamics once actuation begins. Following the strategy for the mesoswimmers presented in our earlier work[43], we also include the beads' masses $m_i = 4/3 a_i^3 \rho_b \pi$ and moments of inertia $I_i = 2/5 a_i^2 m_i$. The ensuing equations of motion are given by

$$\begin{pmatrix} m_i \ddot{\boldsymbol{r}}_i \\ I_i \ddot{\phi}_i \end{pmatrix} = \sum_{j=1}^{7} \begin{pmatrix} \hat{R}_{ij}^{tt} & \hat{R}_{ij}^{tr} \\ \hat{R}_{ij}^{rt} & \hat{R}_{ij}^{rr} \end{pmatrix} \cdot \begin{pmatrix} \dot{\boldsymbol{r}}_j \\ \dot{\phi}_j \end{pmatrix} + \begin{pmatrix} \boldsymbol{F}_i^c \\ 0 \end{pmatrix} + \begin{pmatrix} \boldsymbol{F}_i^m \\ T_i^m \end{pmatrix}, \quad (4)$$

with $\hat{R}$, the resistance matrix calculated in detail in Appendix A.

The parameters for solving equations of motion are obtained from experiments. This includes the remanent moments of $\mu_{\text{rem}} = 9.35 \cdot 10^{-9}$ A m^2 for the bead of diameter 800 μm and to $\mu_{\text{rem}} = 2.3 \cdot 10^{-9}$ A m^2 for the beads of diameter 500 μm. These remanent moment values can drift slightly with storage conditions and usage history, leading to differences in the effective magnetic torques. Importantly, these experimental values represent the in-plane components of the remanent magnetic moments. Consistently, we impose in the simulations that the remanent moment is parallel to the interface plane by choosing in-plane initial conditions and the assumption that the beads can only rotate in-plane. All beads are initialized with zero velocities in a six-fold symmetric structure with the large central bead at the origin. The initial remnant moments of the beads are oriented parallel to the initial horizontal magnetic field. Equations of motion (4) are solved numerically using an algorithm with adaptive step size as implemented in *Mathematica*[50].

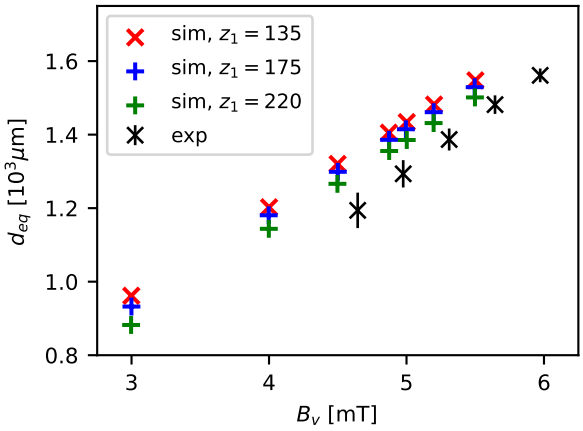

FIG. 3. **Equilibrium distance between two neighboring beads in the seven-bead assembly.** Experimental data (black symbols) are compared with simulations for different deformations of the interface by the central bead.

C. Equilibrium configuration

The application of only the vertical field balances capillary and magnetic forces, allowing the seven-bead system to find an equilibrium configuration with a six-fold symmetry, as shown in Figure 2. For example, for $B_v = 4.98$ mT in the equilibrium configuration, the center-center distance between the outer beads and the central bead is measured 1293 μm while for for $B_v = 5.31$ mT we find 1386 μm.

Experimental and theoretical results show that the equilibrium distance d_{eq} increases linearly with B_v due to the increasing magnetic repulsion, as shown in Figure 3. However, to obtain quantitative agreement between measurements and calculations, capillary interactions had to be approximated to depend only on the projection $\boldsymbol{r}_{ij}^{\parallel}$ onto the liquid interface, while the extent of the z-displacement of the central bead (z_1) was left as a constrained parameter. Deviations of less than 10 % from the experiments are found only after relatively strong deformation of the interface is considered theoretically ($150 < z_1 < 250$ μm). This is consistent with previous findings where the maximum limit for z_1 was independently found to be 330 μm[47].

When a horizontal magnetic field B_h is applied, the angles between $\boldsymbol{r}_{ij}$ and the magnetic field differ for particles positioned to the left or right of the large particle. This asymmetry is depicted in Figure 2(c), which highlights the difference in angles between β_5 and β_2. This asymmetry, arising solely from the height difference z_1, alters the magnetic repulsion and, consequently, the equilibrium distances for particles 5 and 2. This mechanism is crucial for generating the arm compression and extension that leads to motion[43,47].

D. Assembly's eigenmodes and the decomposition of deformations

To understand the motion of the assembly, we determine its 14 eigenmodes: two translations, one rotation, 11 deformations, illustrated in Figure 4. Specifically, we consider the assembly in a constant vertical magnetic field and calculate linear magnetocapillary forces associated with an infinitesimal bead displacement in the xy-plane, which returns a 14×14 stiffness matrix $\underline{K}$. To account for the inertial response of the beads, we define the mass matrix $\underline{M}$ as

$$\underline{M} := \begin{pmatrix} m_1 & 0 & \dots & 0 & 0 \\ 0 & m_1 & 0 & \dots & 0 \\ \vdots & \vdots & \ddots & \vdots & \vdots \\ 0 & \dots & 0 & m_7 & 0 \\ 0 & \dots & 0 & 0 & m_7 \end{pmatrix}, \tag{5}$$

which maps bead accelerations to inertial forces.

The eigenmodes of the system, therefore, correspond to solutions of the generalized eigenvalue problem

$$\left(\underline{K} - \omega^2 \underline{M}\right) \boldsymbol{u} = 0, \tag{6}$$

where $\boldsymbol{u}$ is the eigenvector representing the mode shape associated with the eigenfrequencies $f = \omega/(2\pi)$. The resulting eigenmodes and the associated eigenfrequencies are presented in Figure 4. We find four pairs of degenerate deformation eigenmodes associated with the same eigenfrequencies, with the first pair, consisting of modes 1 and 2, appearing at the highest eigenfrequency. For typical experimental conditions, i.e., device subject to $B_v = 4.9$ mT), this largest eigenfrequency is 5.6 Hz. Each pair of degenerate eigenmodes spans a two-dimensional subspace, chosen as two linearly independent modes of the highest possible symmetry. The 11 eigenmodes are used to decompose the xy-plane deformation of the assembly along its trajectory in its own frame of reference, by systematically calculating the translational and rotational motion of the assembly. The full procedure used to extract bead displacements in this frame is detailed in Appendix B. Such an analysis will prove itself useful in the study of the mesoscopic motions of the assembly.

III. FORCE PROTOCOLS FOR 1-ARM AND 2-ARM METACHRONAL COORDINATION

A. Inducing the assembly rotation

To reconstitute the metachronal motion, we start with a simple rotating magnetic field of the form

$$B_x = B_h \cos(2\pi f t),\ B_y = B_h \sin(2\pi f t), \tag{7}$$

with f the frequency and $B_h = 0.74$ mT the magnitude of the horizontal field.
Conservation of torque naturally implies that the device experiences a net rotation. Our calculations, furthermore, reveal that each bead also rotates around the z-axis as a consequence of its remanent magnetic moment coupling to the external $\boldsymbol{B}$-field as observed in Figure 5(a). These rotations cannot be resolved in experiments due to the symmetry of the beads.

In addition, the outer beads move both inward and toward the next outer bead in the direction of rotation of the magnetic field, as depicted in Figures 5(a) and 5(b). Due to the breaking of the axis-symmetry of the dipole-dipole interactions, we observe metachronal arm compressions and extensions, traveling in a rotating fashion around the assembly (see Movie 1 uploaded to Zenodo[51]). While some level of pumping is achieved, translations are not present as there is no net force and because the device is rotationally symmetric.

B. Inducing the self-propulsion

A precondition for force-free self-propulsion is 2-arm metachronal coordination, which is achieved by doubling the frequency along the y-axis to achieve a Lissajous-type field of the form

$$B_x = B_h \cos(2\pi f t),\ B_y = B_h \sin(4\pi f t). \tag{8}$$

The result is two waves traveling around the assembly (see Movie 2 uploaded to Zenodo[51]) upon compressions of the as-

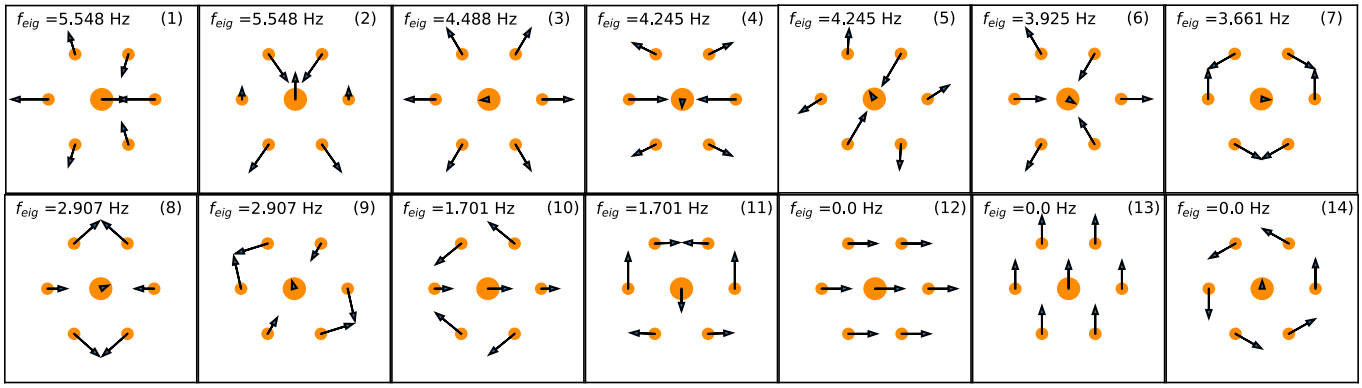

FIG. 4. **Eigenmodes of the seven-bead assembly.** Sketch of the magnetocapillary assembly's eigenmodes with the modes' respective eigenfrequencies.

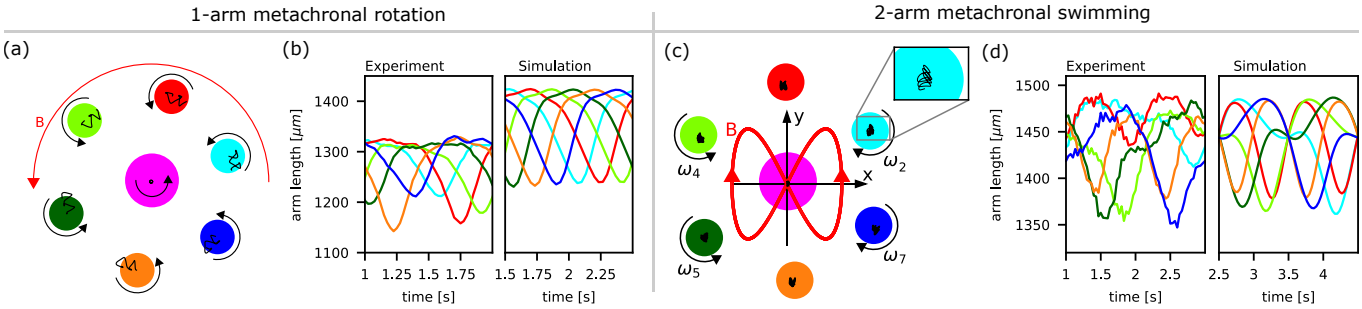

FIG. 5. **Driving protocols for metachronal coordination of a seven-bead assembly.** (a,b) is dedicated to 1-arm metacronal coordination induced by the rotating field. (a) Numerical bead trajectories measured over two periods of the field rotation. The induced bead rotation is depicted by black arrows. (b) Time-dependent arm lengths of the device in the experiments and in the simulations. (c,d) Panels are associated with the 2-arm coordination emerging when applying Lissajous-type magnetic field. (c) Simulated bead trajectories for three periods of the field (the turquoise inset). Side bead rotations are depicted by $\omega_{2,4,5,7}$. (d) The arm lengths of the device in the experiments and in the simulations for $f = 1.0$ Hz, $B_h = 0.5$ mT. Colors of trajectories in (b) and (d) correspond to beads of identical colors in (a) and (c).

sembly and alternate displacement of side arms.

The arms, comprising 2 beads and depicted in blue and green in Figure 5 (c,d), move from the back to the front, with the frequency f of B_x in Eq. (8). In contrast, the distances of the front (red) and the back (orange) beads to the central one oscillate with $2f$, the frequency of B_y. This Lissajous forcing creates two deformation waves that propagate along the structure: one along each lateral arm at frequency f, and another alternating front-to-back compression at frequency $2f$. The alternate compressions can be observed in Figure 5(d). These waves together complete a full cycle over each Lissajous period, resulting in very efficient, force-free, translational locomotion at speeds up to tens of μm/s along the y-direction when $B_h = 1.2$mT. This driving produces a vanishing average torque. Hence, no net rotation of the device is observed, although bead rotation occurs particularly at low frequencies.

C. Maximizing the amplitude of metachronal waves

To understand what determines the amplitude of the metachronal wave, we characterize the deformations of the assembly under both types of magnetic forcings. This requires expressing the deformation of the assembly in terms of the eigenmodes shown in Figure 4 and tracking time-dependent amplitudes of these modes at each frequency of the field. The resulting amplitudes, averaged throughout each assembly trajectory, are shown in Figure 6.

For both 1-arm and 2-arm metachronal coordination (Figures 6(a) and (b), respectively), this reveals that the first two degenerate modes dominate, with additional excitation of modes 4–5 and 10–11. The effect is more substantial under Lissajous forcing due to the higher horizontal magnetic field amplitude $B_h = 1.2$ mT.

For both driving protocols, the amplitude of the deformation modes exhibits a non-monotonic dependence on the field strength. Since the strength of these modes correlates with the intensity of the metachronal wave, an optimal field strength for maximizing wave amplitude is near the point where the principal modes reach their maximum amplitude.

The comparison between simulations and experiments presented in Figure 6(c) for the 2-arm coordination shows very good agreement, which validates the model. The observed differences arise from the restricted time resolution of the experimental video tracking as well as from the effective viscosity reduction at the interface, which enhances excitation amplitudes in experiments. In simulations, we assume the bulk viscosity. This approximation is reasonable as the drag is estimate to be within 10% of the bulk value given that the beads are more than 90% submerged, as previously shown by Delens et al.[47], where for these particles the contact line radius was found to be four times smaller than the bead radius.

D. Cycle-averaged collective dynamics

We now measure and calculate the frequency dependence of the cycle-averaged angular velocity Ω for the 1-arm (Figure 7(a)), and the swimming velocity V in the 2-arm metachronal coordination pattern (Figure 7(b)). Experimental and numerical results exhibit very good agreement over the entire frequency range for both driving protocols, consistent with the agreement of mode decomposition observed in Figure 6(c), strengthening the conclusion that our theoretical approach captures the physics underlying the experimental observations. Residual discrepancies stem from slight variations in bead placement during experiments, lightly affecting z_1 from trial to trial. As the contact line is pinned to the bead, its placement can also affect the in-plane component of μ_{rem} which has an effect on the rotation of the bead.

Consistently, simulations further reveal that both velocities tend to increase with the amplitude of the interface deformation, quantified by z_1 (Figure 2(c)). This trend is illustrated in Figure 7(a), where the rotational velocity Ω under 1-arm forcing increases when comparing $z_1 = 165$ μm (red dots), $z_1 = 200$ μm (blue), and $z_1 = 220$ μm (green).

For both driving protocols, we systematically observe a low- and a high-frequency regime. At low frequencies, we

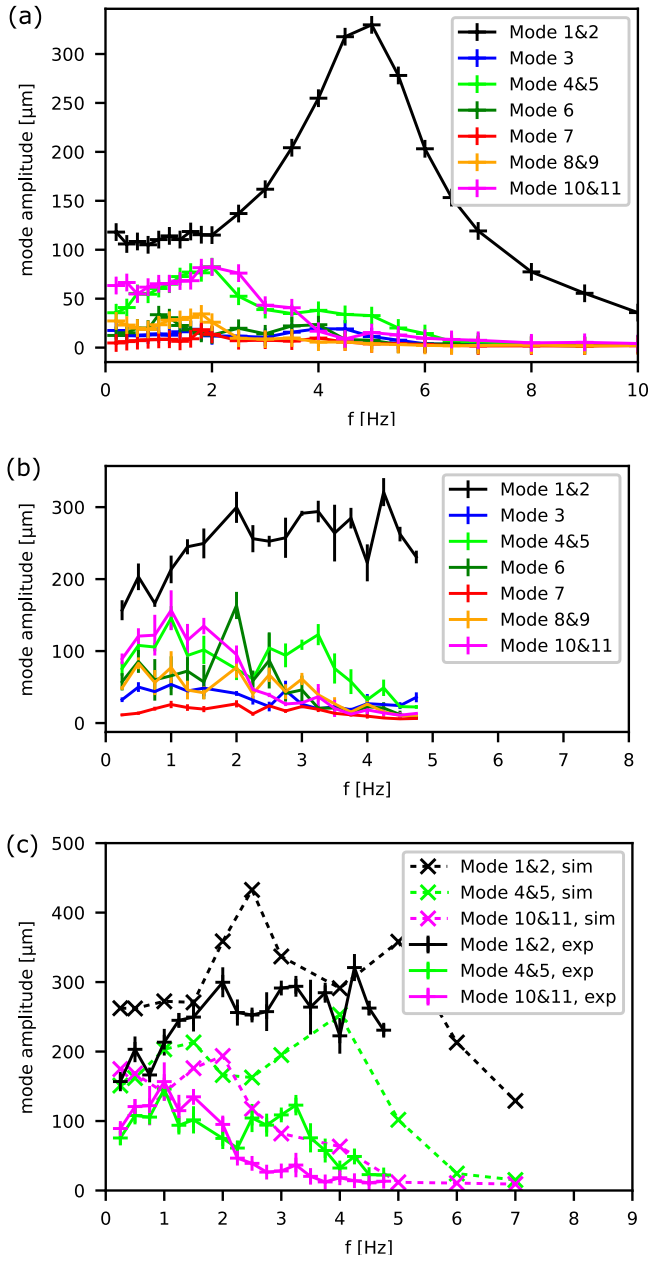

FIG. 6. **Decomposition of the bead assembly deformation into eigenmodes.** Degenerate eigenmodes associated with the same eigenvalue are combined into a single curve. Figures (a) and (b) show the frequency dependence of modes appearing in experiments with a rotating and Lissajous magnetic fields, respectively. Figure (c) compares the excitation of the three main modes between experiments (pluses, solid lines) and simulations (crosses, dashed lines) under Lissajous driving. The lines are a guide for the eye.

find a linear increase of Ω and V towards a peak, which in experiments appears at $f \approx 1-2$ Hz (black crosses in Figure 7). At high frequencies, we find experimentally and in simulations another peak at around 5 Hz. The peak in self-propulsion velocity is at somewhat lower frequencies than with rotational $\boldsymbol{B}$-fields, because of the frequency doubling of the magnetic field in y-direction. The depth difference z_1 influences the interaction, as it creates an asymmetry in the magnetic interaction between the left and right beads and the central bead. The larger z_1 is, the greater the asymmetry and the stronger the associated restoring force, leading to increased rotation and propulsion speed. In the simulations, z_1 modifies the deformation forces through the stiffness matrix $\underline{K}$, which in turn affects the eigenfrequencies shown in Figure 4. These frequencies should therefore exhibit some sensitivity to z_1. However, Figures 6(c) and 7 show that the location of the high-frequency peaks remains nearly unchanged, indicating that the observed dynamics are robust across the tested range of z_1. Interestingly enough, the low-frequency peak is not affected by z_1.

IV. MECHANISMS OF COOPERATIVE MOTION OF THE ASSEMBLY

To understand the origin of this complex frequency response, we resort to a theoretical analysis of the device motion. Our calculations allow us to evaluate one by one the role of different mechanical degrees of freedom on the collective dynamics. For example, tuning the vertical deformation of the interface modulates the strength of hydrodynamic interactions, as shown already in Figure 7(a). Rotation of individual beads can be suppressed by setting the remanent magnetic moment to zero. Deformations are suppressed by setting the horizontal magnetic field strength to zero in the force calculations, thus suppressing bead displacements while retaining a non-zero horizontal component for the torques, allowing bead rotations to persist. Inertial effects can be evaluated by setting the mass of each bead to zero. By comparing such constrained simulations to unconstrained simulations, we isolate the contribution of each modality as discussed in the following sections.

A. The low frequency regime

1. *Interplay of rotations and deformations*

We now apply the procedure with the suppression of bead rotations and arm deformations to both driving protocols. In the low-frequency regime, we find that the emergent collective behaviors—namely, the rotation of the assembly (Figure 8(a)) and its self-propulsion (Figure 8(b)), remain present when deformations are disabled (green symbols), closely matching the full simulations (black symbols). However, when bead rotations are suppressed (red symbols), both rotation and propulsion vanish entirely. These results indicate that rotational degrees of freedom of individual beads and the resulting hydrodynamic flows, rather than deformations, are the primary mechanism driving collective motion at low frequencies.
Under the 1-arm metachronal driving, hydrodynamic interactions transform the local torques applied to individual beads into net mesoscale rotation of the assembly, with minimal contribution from bead displacements. In the 2-arm Lissajous driving, periods during which the beads' orientations follow

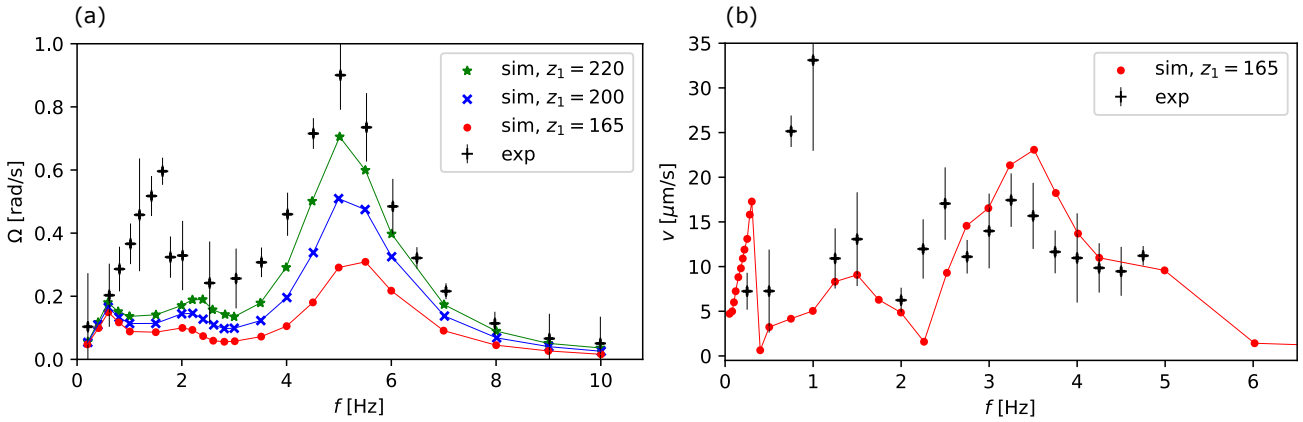

FIG. 7. **Low- and high-frequency regime: comparison of simulations and experiments.** Frequency-dependent angular velocity (a) and self-propulsion velocity (b) for 1-arm and 2-arm metachronal driving with $B_h = 0.742$ mT and $B_h = 1.2$ mT, respectively. Experiments are denoted by black crosses, while simulations are represented by red, blue, and green markers, corresponding to varying depths of the central bead, z_1. The lines are a guide for the eye.

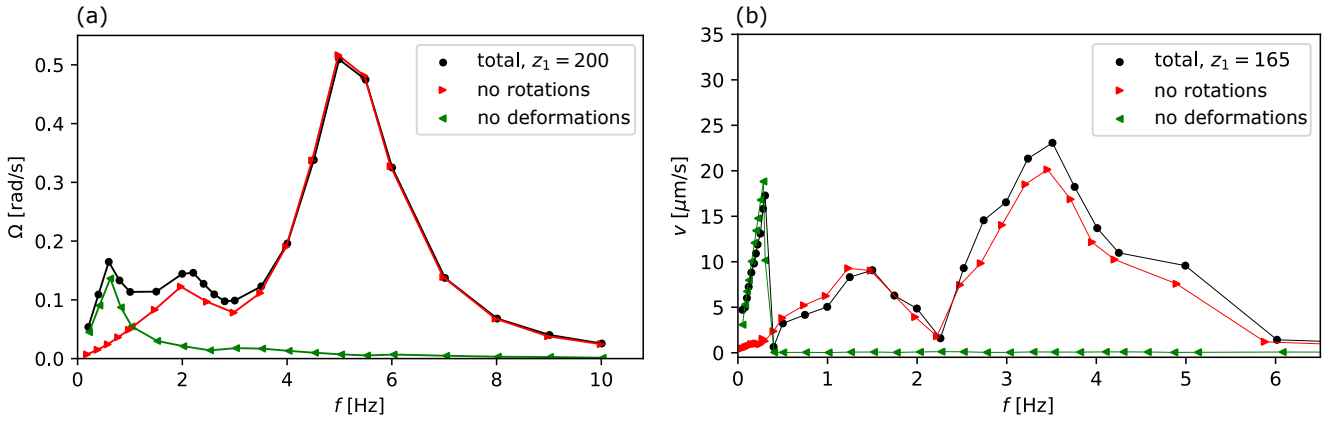

FIG. 8. **Effects of bead rotations and arm deformations on assembly dynamics.** Frequency-dependent rotation speed (a) and translational speed (b) of the magnetocapillary assembly in the rotating (a) and Lissajous (b) magnetic field in the full simulations (black dots), in the absence of forces deforming the assembly (green left-pointing triangles) and in the absence of remnant moments (red right-pointing triangles). The lines are a guide for the eye.

the magnetic field alternate with periods where the field is weak and the bead rotations result from the magnetic dipole-dipole interactions of the beads (see Appendix C for details of the stroke). While a strong external magnetic field leads to bead rotations in the same direction for all beads, the dipole-dipole interactions at instants of a weak external field are roughly axis-symmetric with respect to the preceding orientation of the external magnetic field. This leads to a breaking of the rotational symmetry and enables swimmer translation in a force-free manner.

The dominant contribution comes from the four lateral beads oriented along the swimmer's direction of motion (blue and green beads in Figure 5(c)). These beads rotate continuously in the same direction, providing rotlets that produce a net flow in the positive y-direction and propel the swimmer forward. This effect can be observed in Figure 9(b) where we show the linear dependence of the swimming speed to the average angular velocities of the four side beads at low frequency. This confirms that self-propulsion at low frequencies is purely driven by rotations and hydrodynamic interactions between the beads.

2. Phase locking to the magnetic field and the contribution of hydrodynamic interactions

Now that bead rotation has been identified as the key mechanism in the low-frequency regime, we turn to explain the observed linear increase towards a peak in both rotational and propulsion speeds in Figures 7 and 8. Due to the linear torque response of the beads with the magnetic field, the rotlet strength and thus both the rotation and propulsion speed,

Ω and V, increase with frequency. As the frequency increases further, the bead rotations can no longer follow the field, and Ω and V drop. We, therefore, find that the position of the low-frequency peak can be associated with the step-out frequency. This frequency corresponds to the moment the load torque of the bead, necessary to keep it rotating at a constant speed, and depending on the viscosity of the system, equals the magnetic torque[52].
Therefore, we found

$$f_{so,i} = \frac{1}{2\pi} \frac{|\boldsymbol{\mu}_{rem,i}| B_h}{8\pi\eta a_i^3}, \tag{9}$$

which, for the theoretical model, is calculated as $f_{so} \approx 0.7$ Hz. The higher step-out frequency observed experimentally results from the decreased hydrodynamic friction due to partial bead immersion in the fluid. Indeed, as shown in Figure 9, by theoretically scaling down the hydrodynamic friction (first term in Eq. (4)), the linear regime is also extended numerically.

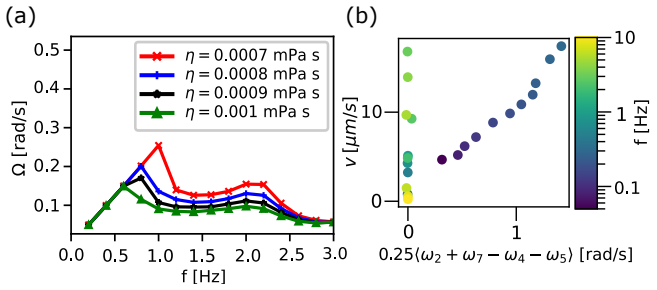

FIG. 9. **Characteristics of the low frequency regime.** (a) Frequency-dependent rotation speed of different values of the viscosity. A decrease in viscosity is accompanied by an increasing step-out frequency f_{so}. (b) Dependence of swimming speed in the y-direction on the average angular velocities $\omega_{2,4,5,7}$ of the four side beads of the assembly. At low frequencies, a linear relation is observed, suggesting that swimming speed and bead rotation are proportional.

B. The high frequency regime

1. *Interplay of rotations and deformations*

A very different origin of motion is found at high frequencies, where beads no longer follow the field. Figure 8 shows that at higher driving frequencies (above 2 Hz for the rotating field (Figure 8(a)) and in the $3-5$ Hz range for Lissajous driving Figure 8(b)), the respective global motions persist even in the absence of remanent magnetic moments (red symbols), but vanish when deformations are disabled (green symbols). In the case of Lissajous driving, the results are consistent with Figure 9(b), showing that the average rotation speed of the side beads drops to zero after reaching the step-out frequency, whereas the propulsion speed remains unaffected.

These results confirm that, in the high-frequency regime, propulsion is no longer driven by individual bead rotations but rather emerges from collective, deformation-driven dynamics. In fact, these motions result from the metachronal coordination of bead displacements within the interface plane, which dominates the assembly's response in this regime. The global motion observed is thus a consequence of coherent shape changes of the assembly rather than local torque-induced effects.

2. *The role of inertia in metachronal coordination*

Given the considerable speed of the device, it is instructive to verify the characteristic Reynolds numbers[43,53]. For the fluid, with L being the total length of the device, and η the fluid viscosity, $Re_f = \rho L v/\eta \approx 0.09$, which is well within the low Re regime. On the other hand, the assembly's Reynolds number is $Re_s = 2\pi\rho_b a_i^2 f/\eta \approx 10-30$ near the resonance. This points to the fact that the swimmer's inertia likely plays an important role in metachronal coordination and highlights the mesoscale nature of the assembly in this regime.

To demonstrate the importance of inertia, we repeat the calculation by setting the bead masses to zero (blue stars in Figure 10). Concomitantly, high-frequency peaks are lost, both for the rotational and Lissajous driving, while metachronal coordination persists, although at much lower amplitudes. This demonstrates that these peaks result from the inertial translations of the beads in the xy-plane. We therefore return to the modal analysis of assembly deformation shown in Figure 6. We find that two main deformation modes, associated with the eigenfrequency of 5.5 Hz, are excited near the high-frequency peak. This is in excellent agreement with the maximal swimming speed observed in both experiments and calculations. We conclude that this regime peak is indeed associated with a mechanical resonance induced by the inertia of the magnetocapillary system. Consistent with the frequency doubling of the magnetic field in y-direction, the peak for translational self-propulsion is at lower frequencies than with rotational $\boldsymbol{B}$-fields. Given the Reynolds numbers, the surrounding fluid remains in a low Reynolds number regime and the flow is expected to stay laminar and inertia-less throughout. As such, the transition between low- and high-frequency regimes does not correspond to a qualitative change in the flow structure but rather reflects the increasing role of bead inertia and deformation dynamics in driving propulsion. This interpretation is consistent with previous work on mesoscale swimmers, which showed that even in low Reynolds number fluids, the swimmer's own inertia can enable propulsion by breaking time-reversal symmetry[43].

V. CONCLUSION

In this work, we reconstituted metachronal coordination, characterized by sequential oscillatory translations of individual components, in a minimal model system composed of seven beads. We systematically examined how magnetic, capillary, and hydrodynamic interactions, in conjunction with inertial effects, give rise to cooperative motion. This assembly served as a model platform to identify two distinct regimes of

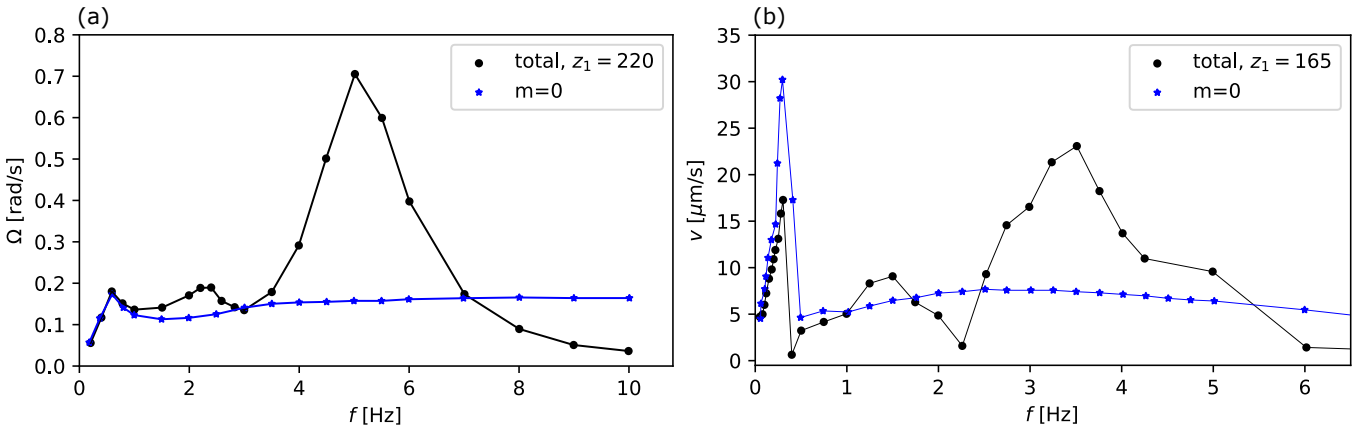

FIG. 10. **Effects of inertia.** Comparison of results of full simulations (black dots) with simulations with the mass of beads set to zero (blue stars). Only the low-frequency regime, i.e., small *Re* regime, was recovered in both the case of rotational (a) and Lissajous magnetic field (b), confirming that inertia plays an important role in metachronal coordination.

locomotion, governed by the driving frequency of the external forcing.

At low driving frequencies, we find that metachronal coordination, while present, is not the primary mechanism responsible for the cooperative motion of the assembly. In this regime, propulsion arises primarily from rotlet-induced flows driven by bead rotations, rather than from collective deformation dynamics. The observed dynamics are consistent with a class of theoretically proposed devices in which active components generate flow fields that act on passive parts of the system, thereby producing net locomotion[54,55]. Accordingly, the Reynolds numbers associated with the motions of appendages, the assembly, and the fluid are very low, and the system is in the so-called viscous-dominated regime. In our experimental implementation, this concept is realized through the linear coupling of the external magnetic field $\boldsymbol{B}$ to the remanent magnetic moments of the beads, resulting in bead rotations that closely follow the oscillating field. Depending on the chosen driving protocol, this can lead to efficient rotation and directed translation of the entire assembly.

At high driving frequencies, metachronal organization becomes essential for self-propulsion. In this regime, the Reynolds number of the assembly spans from fluid-dominated values ($\ll 1$) to mesoscopic values exhibited by moving body parts (1–10), especially near its mechanical resonance. In our model system, this transition is reflected in the amplification of the swimming stroke due to bead inertia, as confirmed by quantitative agreement between experiment and theory.

For organisms on the micro and mesoscale, these results suggest that employing high-density components provides a promising strategy to overcome the slow locomotion in highly viscous environments. An alternative strategy is fast actuation, which is indeed commonly associated with metachronal coordination, for example, in beating cilia. Larger organisms, such as krill[56] and jellyfish[57], naturally access the mesoscopic regime due to their size. In these systems, optimizing self-propulsion while minimizing energetic cost has been directly linked to resonance phenomena[58], an idea further supported by analogies with damped harmonic oscillators[59]. Similar resonance-enhanced swimming strategies have also been demonstrated in bio-inspired flapping and flexible foil systems, where structural compliance and fluid–structure interactions tune propulsion performance[60,61]. Our observation that swimming speed peaks near a mechanical resonance echoes these biological and engineered strategies: in both natural and artificial systems, locomotion is enhanced when actuation aligns with an optimal flapping frequency.

Additional investigation is, however, necessary to establish the broader relationship between metachronal coordination and inertial effects across diverse biological contexts. Our work contributes a comprehensive phenomenological framework that elucidates how mechanical degrees of freedom, coupled with hydrodynamic and inertial effects, govern emergent motion across a wide parameter space, provided the flow remains within the laminar regime. Our findings, therefore, may be relevant to understanding the common occurrence of metachronal coordination in nature.

Together, these two propulsion regimes – hydrodynamic interaction-driven motion yielding microswimming, and resonance-enhanced inertial motion accessing the mesoscale – offer complementary design strategies for synthetic swimmers and microfluidic actuators. By combining dense components with coordinated actuation such as metachronal waves, future devices could adaptively switch between mechanisms depending on scale, fluid environment, or functional demands. This dual-mode framework opens new avenues for engineering agile, energy-efficient systems capable of pumping and navigating complex fluidic landscapes with biological-level sophistication.

ACKNOWLEDGMENTS

This work is financially supported by the FNRS CDR project number J.0186.23 entitled “Magnetocapillary Interactions for Locomotion at Liquid Interfaces" (MILLI). Further support was provided by the Deutsche Forschungsgemeinschaft project 416229255 SFB 1411 Design of Particulate Products. NV thanks the Francqui Foundation (Brussels) for financial support.

DATA AVAILABILITY STATEMENT

The data that support the findings of this study are openly available in the Zenodo repository at https://zenodo.org/records/15680310[51].

Appendix A: Numerical methods

In the simulations, the bulk low Reynolds number hydrodynamics at the level of the Rotne-Prager approximation, i.e., including all terms up to the order $\mathcal{O}(a/r)^3$, is used. Since at the Rotne-Prager level, the expressions for the mobility matrix $\hat{\mu}$ are simpler than for the resistance matrix $\hat{R} = -\hat{\mu}^{-1}$[62], we implement in the simulations the mobility matrix and invert it later. The corresponding expressions for components of the mobility matrix are[63,64]:

$$\begin{aligned}
\hat{\mu}_{ij}^{tt} &= \frac{1}{8\pi\eta|\boldsymbol{r}_{ij}|}\left(\hat{1}+\frac{\boldsymbol{r}_{ij}\otimes\boldsymbol{r}_{ij}}{|\boldsymbol{r}_{ij}|^2}\right)+ \\
&\qquad \frac{a_i^2+a_j^2}{24\pi\eta|\boldsymbol{r}_{ij}|^3}\left(\hat{1}-3\frac{\boldsymbol{r}_{ij}\otimes\boldsymbol{r}_{ij}}{|\boldsymbol{r}_{ij}|^2}\right)\ (i\neq j), \\
\hat{\mu}_{ii}^{tt} &= \frac{\hat{1}}{6\pi\eta a_i}, \\
\hat{\mu}_{ij}^{tr} &= \frac{1}{8\pi\eta|\boldsymbol{r}_{ij}|^3}(\boldsymbol{r}_{ij}\times)\ (i\neq j),\ \hat{\mu}_{ii}^{tr}=\hat{0}, \hat{\mu}_{ij}^{rt}=\left(\hat{\mu}_{ji}^{tr}\right)^T, \\
\hat{\mu}_{ij}^{rr} &= 0\ (i\neq j),\ \hat{\mu}_{ii}^{rr}=\frac{1}{8\pi\eta a_i^3}.
\end{aligned} \tag{A1}$$

Here, the upper indices t and r denote translation and rotation, respectively, while i and j refer to two beads of the assembly. The symbol $\otimes$ denotes the tensor product of two vectors and $(\boldsymbol{r}_{ij}\times)$ is a rank-two tensor defined as

$$(\boldsymbol{r}_{ij}\times) := \varepsilon_{pqr}\left(\boldsymbol{r}_{ij}\right)_q \boldsymbol{e}_p\boldsymbol{e}_r, \tag{A2}$$

with ε the Levi-Civita symbol, p,q,r spatial indices, and $\boldsymbol{e}_p$ the unit vector in the direction associated with the index p. The water viscosity η is assumed as $\eta = 1.0$ mPa s.

Since we consider rotations only around the z-axis, we use for the components of the mobility matrix of the form $\hat{\mu}_{ij}^{tr}$, $\hat{\mu}_{ij}^{rt}$ and $\hat{\mu}_{ij}^{rr}$ only the entries associated with rotation about the z-axis. For instance, $\hat{\mu}_{ij}^{rr}$ then becomes a scalar while $\hat{\mu}_{ij}^{tr}$ and $\hat{\mu}_{ij}^{rt}$ are represented as tensors of dimensionality 3×1 and 1×3, respectively.

We then define the full mobility matrix as

$$\hat{\mu} = \begin{pmatrix}
\hat{\mu}_{11}^{tt} & \dots & \hat{\mu}_{17}^{tt} & \hat{\mu}_{11}^{tr} & \dots & \hat{\mu}_{17}^{tr} \\
\vdots & \ddots & \vdots & \vdots & \ddots & \vdots \\
\hat{\mu}_{71}^{tt} & \dots & \hat{\mu}_{77}^{tt} & \hat{\mu}_{71}^{tr} & \dots & \hat{\mu}_{77}^{tr} \\
\hat{\mu}_{11}^{rt} & \dots & \hat{\mu}_{17}^{rt} & \hat{\mu}_{11}^{rr} & \dots & \hat{\mu}_{17}^{rr} \\
\vdots & \ddots & \vdots & \vdots & \ddots & \vdots \\
\hat{\mu}_{71}^{rt} & \dots & \hat{\mu}_{77}^{rt} & \hat{\mu}_{71}^{rr} & \dots & \hat{\mu}_{77}^{rr}
\end{pmatrix}. \tag{A3}$$

Inverting this expression gives rise to the components of the resistance matrix $\hat{R}$ that are used in Eq. (3) of the main text.

Appendix B: Decomposition of the assembly deformation

For the decomposition of the assembly deformation in eigenmodes, the displacement of each bead in the device's frame of reference is required for each instant of time. Since the beads cannot move in the z-direction by assumption, we restrict our focus to the x- and y-components of the bead position vectors $\boldsymbol{r}_k$. We calculate the assembly orientation for each time step by

$$\alpha_s = \arg\left(\sum_{k=2}^{7}\exp\left(i(\alpha_k - \frac{2\pi}{6}(k-2)\right)\right), \tag{B1}$$

with α_k the orientation of $\boldsymbol{r}_k - \boldsymbol{r}_1$, i.e. the orientation of the arm associated with bead k, with $k\in\{2,...,7\}$, and arg the argument of a complex number. We then calculate the center of mass

$$\boldsymbol{r}_{COM} := \frac{\sum_{k=1}^{7} m_k \boldsymbol{r}_k}{\sum_{k=1}^{7} m_k}, \tag{B2}$$

as well as the rotated bead positions such that the average assembly orientation is zero and the center of mass is in the origin of the coordinate system,

$$\boldsymbol{r}_k' = \begin{pmatrix}\cos(-\alpha_s) & -\sin(-\alpha_s)\\ \sin(-\alpha_s) & \cos(-\alpha_s)\end{pmatrix}\cdot(\boldsymbol{r}_k - \boldsymbol{r}_{COM}). \tag{B3}$$

The bead displacement is then calculated as the difference between each $\boldsymbol{r}_k'$ and the symmetric six-fold structure with the central bead in the origin and all other bead positions defined by

$$\boldsymbol{r}_k^{eq} = l^{eq}\left(\cos\left(\frac{2\pi}{6}(k-2)\right), \sin\left(\frac{2\pi}{6}(k-2)\right)\right)^T. \tag{B4}$$

Here, l^{eq} denotes the assembly's time-averaged arm length.

Appendix C: Stroke of the 7-bead assembly during self-propulsion

At low frequencies, we find that the assembly rotation results from continuous rotations of outer beads around the z-axis. In Figure 11, we sketch the mechanism that leads to

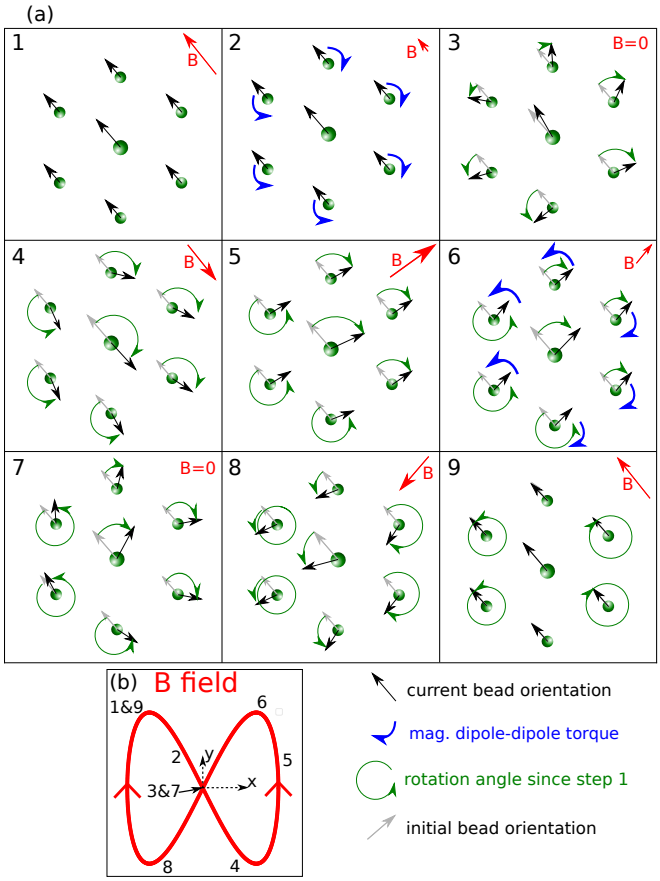

FIG. 11. Swimming mechanism of the seven-bead assembly in the low-frequency regime. (a) Sketch of the orientations of the remanent moments during one full cycle of the Lissajous-type horizontal magnetic field. (b) Plot of the Lissajous field, with the $\boldsymbol{B}$-field of the different snapshots in part (a) indicated.

the single bead rotations in the simulations. Here, the black arrows indicate the current bead orientation while the green arrows indicate the cumulative rotation since step 1. The pale gray arrows indicate the initial bead orientation, and the blue arrows indicate dipole-dipole torques.

In detail, when the horizontal magnetic field switches direction, the three beads on the lower left side rotate counterclockwise (CCW), while the others rotate clockwise (CW) (Figure 11, step 2). After the external field has switched direction (step 3), all beads follow the CCW rotation of the external field (step 5). When the horizontal field switches direction again (steps 6 and 7), the orientation of the remanent bead moments is again aligned with the preceding orientation of the magnetic field, which is, however, different from that of the first switching event. As a consequence, the three beads on the upper left side rotate CCW while the beads on the lower left side rotate CW. After the horizontal field has switched direction, all beads again follow the CW rotation of the magnetic field.

After a full cycle of the Lissajous-type magnetic field, the two beads on the swimmer's left side have performed a full CCW rotation, while the beads on the right side have undergone a full CW rotation. The resulting flow field points upwards at the central bead as well as at the beads above and below it. Consequently, this leads to upward swimming of the magnetocapillary ensemble.

REFERENCES

[1] E. M. Purcell, "Life at low reynolds number," American journal of physics **45**, 3–11 (1977).

[2] E. Lauga, "Bacterial hydrodynamics," Annu. Rev. Fluid Mech. **48**, 105–130 (2016).

[3] E. Lauga and T. R. Powers, "The hydrodynamics of swimming microorganisms," Rep. Prog. Phys. **72**, 096601 (2009).

[4] M. Byron, A. Santhanakrishnan, and D. Murphy, "Metachronal Coordination of Multiple Appendages for Swimming and Pumping," Integr. Comp. Biol. **61**, 1561–1566 (2021).

[5] H. Machemer, "Ciliary activity and the origin of metachrony in Paramecium: effects of increased viscosity." J. Exp. Biol. **57**, 239–259 (1972).

[6] N. Narematsu, R. Quek, K. H. Chiam, and Y. Iwadate, "Ciliary metachronal wave propagation on the compliant surface of Paramecium cells," Cytoskeleton **72**, 633–646 (2015).

[7] D. R. Brumley, M. Polin, T. J. Pedley, and R. E. Goldstein, "Hydrodynamic synchronization and metachronal waves on the surface of the colonial alga Volvox carteri," Phys. Rev. Lett. **109**, 268102 (2012).

[8] M. J. Sanderson and M. A. Sleigh, "Ciliary activity of cultured rabbit tracheal epithelium: beat pattern and metachrony," J. Cell Sci. **47**, 331–347 (1981).

[9] L. B. Wong, I. F. Miller, and D. B. Yeates, "Nature of the mammalian ciliary metachronal wave," J. Appl. Physiol. **75**, 458–467 (1993).

[10] O. Mesdjian, C. Wang, S. Gsell, U. D'Ortona, J. Favier, A. Viallat, and E. Loiseau, "Longitudinal to Transverse Metachronal Wave Transitions in an in Vitro Model of Ciliated Bronchial Epithelium," Phys. Rev. Lett. **129**, 038101 (2022).

[11] S. L. Tamm, "Cilia and the life of ctenophores," Invertebr. Biol. **133**, 1–46 (2014).

[12] N. Osterman and A. Vilfan, "Finding the ciliary beating pattern with optimal efficiency," Proc. Natl. Acad. Sci. U.S.A. **108**, 15727–15732 (2011).

[13] A. Vilfan and F. Jülicher, "Hydrodynamic flow patterns and synchronization of beating cilia," Phys. Rev. Lett. **96**, 058102 (2006).

[14] M. Vilfan, A. Potočnik, B. Kavčič, N. Osterman, I. Poberaj, A. Vilfan, and D. Babič, "Self-assembled artificial cilia," Proc. Natl. Acad. Sci. U.S.A. **107**, 1844–1847 (2010), https://www.pnas.org/doi/pdf/10.1073/pnas.0906819106.

[15] J. Elgeti and G. Gompper, "Emergence of metachronal waves in cilia arrays," Proc. Natl. Acad. Sci. U.S.A. **110**, 4470–4475 (2013).

[16] D. Murphy, D. Webster, S. Kawaguchi, R. King, and J. Yen, "Metachronal swimming in antarctic krill: gait kinematics and system design," Mar. Biol. **158**, 2541–2554 (2011).

[17] M. Ruszczyk, D. R. Webster, and J. Yen, "Trends in stroke kinematics, reynolds number, and swimming mode in shrimp-like organisms," Integr. Comp. Biol. **62**, 791–804 (2022).

[18] P. Tierno, R. Golestanian, I. Pagonabarraga, and F. Sagués, "Controlled swimming in confined fluids of magnetically actuated colloidal rotors," Phys. Rev. Lett. **101**, 218304 (2008).

[19] P. Tierno, "Recent advances in anisotropic magnetic colloids: realization, assembly and applications," Phys. Chem. Chem. Phys. **16**, 23515–23528 (2014).

[20] K. J. Solis and J. E. Martin, "Complex magnetic fields breathe life into fluids," Soft Matter **10**, 9136–9142 (2014).

[21] A. Snezhko, M. Belkin, I. Aranson, and W.-K. Kwok, "Self-assembled magnetic surface swimmers," Phys. Rev. Lett. **102**, 118103 (2009).

[22] S. Palagi, E. W. Jager, B. Mazzolai, and L. Beccai, "Propulsion of swimming microrobots inspired by metachronal waves in ciliates: From biology to material specifications," Bioinspir. Biomim. **8**, 046004 (2013).

[23] F. Tsumori, R. Marume, A. Saijou, K. Kudo, T. Osada, and H. Miura, "Metachronal wave of artificial cilia array actuated by applied magnetic field," Jpn. J. Appl. Phys. **55**, 06GP19 (2016).

[24] S. Hanasoge, P. J. Hesketh, and A. Alexeev, "Metachronal motion of artificial magnetic cilia," Soft Matter **14**, 3689–3693 (2018).

[25] X. Dong, G. Z. Lum, W. Hu, R. Zhang, Z. Ren, P. R. Onck, and M. Sitti, "Bioinspired cilia arrays with programmable nonreciprocal motion and metachronal coordination," Sci. Adv. **6**, eabc9323 (2020).

[26] H. Gu, Q. Boehler, H. Cui, E. Secchi, G. Savorana, C. De Marco, S. Gervasoni, Q. Peyron, T. Y. Huang, S. Pane, A. M. Hirt, D. Ahmed, and B. J. Nelson, "Magnetic cilia carpets with programmable metachronal waves," Nat. Commun. **11**, 2637 (2020).

[27] P. Tierno, R. Muruganathan, and T. M. Fischer, "Viscoelasticity of dynamically self-assembled paramagnetic colloidal clusters," Phys. Rev. Lett. **98**, 028301 (2007).

[28] G. Grosjean, G. Lagubeau, A. Darras, M. Hubert, G. Lumay, and N. Vandewalle, "Remote control of self-assembled microswimmers," Sci. Rep. **5**, 16035 (2015).

[29] G. Grosjean, M. Hubert, and N. Vandewalle, "Magnetocapillary self-assemblies: Locomotion and micromanipulation along a liquid interface," Adv. Colloid Interface Sci. **255**, 84–93 (2018).

[30] G. Grosjean, M. Hubert, G. Lagubeau, and N. Vandewalle, "Realization of the Najafi-Golestanian microswimmer," Phys. Rev. E **94**, 021101 (2016).

[31] G. Grosjean, M. Hubert, Y. Collard, A. Sukhov, J. Harting, A. S. Smith, and N. Vandewalle, "Capillary assemblies in a rotating magnetic field," Soft Matter **15**, 9093–9103 (2019).

[32] Y. Collard, G. Grosjean, and N. Vandewalle, "Magnetically powered metachronal waves induce locomotion in self-assemblies," Commun. Phys. **3**, 112 (2020).

[33] D. Vella and L. Mahadevan, "The "Cheerios effect"," Am. J. Phys. **73**, 817–825 (2005).

[34] A. Najafi and R. Golestanian, "A simplest swimmer at low Reynolds number: Three linked spheres," Phys. Rev. E **69**, 062901 (2004).

[35] B. U. Felderhof, "The swimming of animalcules," Phys. Fluids **18**, 063101 (2006).

[36] C. M. Pooley, G. P. Alexander, and J. M. Yeomans, "Hydrodynamic interaction between two swimmers at low reynolds number," Phys. Rev. Lett. **99**, 228103 (2007).

[37] J. Pande and A.-S. Smith, "Forces and shapes as determinants of microswimming: Effect on synchronisation and the utilisation of drag," Soft Matter **11**, 2364–2371 (2015).

[38] M. S. Rizvi, A. Farutin, and C. Misbah, "Three-bead steering microswimmers," Phys. Rev. E **97**, 023102 (2018).

[39] D. Klotsa, K. A. Baldwin, R. J. Hill, R. M. Bowley, and M. R. Swift, "Propulsion of a Two-Sphere Swimmer," Phys. Rev. Lett. **115**, 248102 (2015), 1501.05143.

[40] T. Dombrowski, S. K. Jones, G. Katsikis, A. P. S. Bhalla, B. E. Griffith, and D. Klotsa, "Transition in swimming direction in a model self-propelled inertial swimmer," Phys. Rev. Fluids **4**, 021101 (2019).

[41] S. Ziegler, M. Hubert, N. Vandewalle, J. Harting, and A.-S. Smith, "A general perturbative approach for bead-based microswimmers reveals rich self-propulsion phenomena," New J. Phys. **21**, 113017 (2019).

[42] A. Sukhov, S. Ziegler, Q. Xie, O. Trosman, J. Pande, G. Grosjean, M. Hubert, N. Vandewalle, A.-S. Smith, and J. Harting, "Optimal motion of triangular magnetocapillary swimmers," J. Chem. Phys. **151**, 124707 (2019).

[43] M. Hubert, O. Trosman, Y. Collard, A. Sukhov, J. Harting, N. Vandewalle, and A. S. Smith, "Scallop Theorem and Swimming at the Mesoscale," Phys. Rev. Lett. **126**, 224501 (2021).

[44] A. Sukhov, M. Hubert, G. Grosjean, O. Trosman, S. Ziegler, Y. Collard, N. Vandewalle, A.-S. Smith, and J. Harting, "Regimes of motion of magnetocapillary swimmers," Eur. Phys. J. E **44**, 59 (2021).

[45] D. Gonzalez-Rodriguez and E. Lauga, "Reciprocal locomotion of dense swimmers in Stokes flow," J. Phys.: Condens. Matter **21**, 204103 (2009).

[46] D. Geyer, S. Ziegler, A. Sukhov, M. Hubert, A.-S. Smith, O. Aouane, P. Malgaretti, and J. Harting, "Lattice Boltzmann simulations of two linear microswimmers using the immersed boundary method," Commun. Comput. Phys. **33**, 310–329 (2023).

[47] M. Delens, Y. Collard, and N. Vandewalle, "Induced capillary dipoles in floating particle assemblies," Phys. Rev. Fluids **8**, 074001 (2023).

[48] G. Lagubeau, G. Grosjean, A. Darras, G. Lumay, M. Hubert, and N. Vandewalle, "Statics and dynamics of magnetocapillary bonds," Phys. Rev. E **93**, 053117 (2016).

[49] P. A. Kralchevsky and K. Nagayama, "Capillary interactions between particles bound to interfaces, liquid films and biomembranes," Adv. Colloid Interface Sci. **85**, 145–192 (2000).

[50] Wolfram Research Inc., "Mathematica, Version 12.2," (2020).

[51] S. Ziegler, M. Delens, Y. Collard, M. Hubert, N. Vandewalle, and A.-S. Smith, "Data for Metachronal coordination as a mesoscale phenomenon," Zenodo archive (2025), 10.5281/zenodo.15632606.

[52] A. W. Mahoney, N. D. Nelson, K. E. Peyer, B. J. Nelson, and J. J. Abbott, "Behavior of rotating magnetic microrobots above the step-out frequency with application to control of multi-microrobot systems," Appl. Phys. Lett. **104**, 144101 (2014).

[53] N. J. Derr, T. Dombrowski, C. H. Rycroft, and D. Klotsa, "Reciprocal swimming at intermediate Reynolds number," J. Fluid Mech. **952**, A8 (2022).

[54] C. Hoell, H. Löwen, and A. M. Menzel, "Dynamical density functional theory for circle swimmers," New J. Phys. **19**, 125004 (2017).

[55] C. Hoell, H. Löwen, and A. M. Menzel, "Particle-scale statistical theory for hydrodynamically induced polar ordering in microswimmer suspensions," J. Chem. Phys. **149**, 144902 (2018).

[56] C. Zhang, R. D. Guy, B. Mulloney, Q. Zhang, and T. J. Lewis, "Neural mechanism of optimal limb coordination in crustacean swimming," Proc. Natl. Acad. Sci. U.S.A. **111**, 13840–13845 (2014).

[57] M. E. Demont and J. M. Gosline, "Hmechanics of jet propulsion in the hydromedusan jellyfish, polyorchis penicillatus: Iii. a natural resonating bell; the presence and importance of a resonant phenomenon in the locomotor structure," J. Exp. Biol. **134**, 347–361 (1988).

[58] A. Hoover and L. Miller, "A numerical study of the benefits of driving jellyfish bells at their natural frequency," J. Theor. Biol. **374**, 13–25 (2015).

[59] B. K. Ahlborn, R. W. Blake, and W. M. Megill, "Frequency tuning in animal locomotion," Zoology **109**, 43–53 (2006).

[60] C. L. Shah, D. Majumdar, C. Bose, and S. Sarkar, "Chordwise flexible aft-tail suppresses jet-switching by reinstating wake periodicity in a flapping foil," Journal of Fluid Mechanics **946**, A12 (2022).

[61] C. L. Shah, K. Dhileep, Q. Huang, S. Ravi, and S. Sarkar, "Bio-inspired forward and backward swimming gaits resulting from fluid–structure interactions," in *Proceedings A*, Vol. 481 (The Royal Society, 2025) p. 20240147.

[62] S. Kim and S. J. Karilla, *Microhydrodynamics : Principles and Selected Applications* (Courier Corporation, 1991).

[63] J. K. G. Dhont, *An Introduction to Dynamics of Colloids* (Elsevier, 1996).

[64] K. Pickl, J. Pande, H. Köstler, U. Rüde, and A.-S. Smith, "Lattice Boltzmann simulations of the bead-spring microswimmer with a responsive stroke - From an individual to swarms," J. Phys.: Condens. Matter **29**, 124001 (2017).